Infrared clutter measurements of marine backgrounds

Piet Schwering

TNO Physics and Electronics Laboratory
P.O. Box 96864, NL–2509 JG The Hague, The Netherlands

ABSTRACT

Observations in the infrared wavelength band between 8 and 12μm of sea backgrounds have been recorded with a CCIR compatible imager for a large number of sea states (0 – 6). Recordings took place in coastal areas as well as on open seas. The behaviour of clutter in the infrared data was analyzed in space and in time. Clutter values are analyzed to give estimates for the physical appearance of the sea, such as wave structure. Elevation profiles are evaluated for sea state characteristics and show that the variation of the RMS with elevation ($-\mathrm{dRMS}/\mathrm{d}\epsilon$) decreases with increasing sea state number. Infrared sequences are used to derive periods in the RMS clutter values and to derive time constants of about 1 second for the images in the sequence to become uncorrelated. A constant azimuthal wave velocity is found from the radiance images. Sunglint images were recorded with FEL–TNO's Multi Path Transmissometer Radiometer (MPTR) simultaneously in six wavelength bands at 0.6, 0.8, 1.3, 2.1, 4.0 and 10.0μm in coastal areas. The presented images are very similar in all six bands with a pattern width of 8.8°. The elevation averaged profiles are well fitted by a Gaussian pattern. Characteristic hotspot duration times were estimated to be 0.15 to 0.20 seconds. The spectral correlation is investigated and found to be present only on a global scale.

1. INTRODUCTION

Each object with a temperature above the absolute zero will radiate thermal energy according to Planck's law. This radiation law is weighed by the emission coefficient of the object and, together with the reflected surroundings of the object, transmitted through a medium before it is detected by the observer. For background objects (300 K) the peak of the Planck radiation law is at wavelengths near 10μm, while hot (700 K) objects peak at 4 μm. The Earth's atmosphere is relatively transparant in bands at these wavelengths. Due to its physical nature, infrared radiation is a means of observing objects at night (mainly emission) as well as during day times (emission and reflection). Therefore imagers and surveillance systems that operate in the infrared wavelength bands at 3 – 5 μm or 8 – 12 μm are used in a variety of fields.

Both infrared imagery and surveillance systems that are used for point target detection are hampered by clutter. Clutter results in false alarms and should therefore be reduced. In this paper we estimate characteristics of clutter by means of physical appearances of maritime infrared scenes. With the use of data recorded at various locations we investigate the relation between infrared clutter and sea states, infrared clutter with respect to elevation and clutter in relation to sunglint.

Our analysis is based on infrared imagery. In order to quantify the term clutter in infrared images we calculate the RMS in image areas, defined as RMS $= \sqrt{<(I - <I>)^2>}$, where $< .. >$ denotes averaging over the specific image area and I represents the infrared radiance in the images. Point target filters that

are applied to images often consider a local area (*e.g.* 3x3 Laplace filters). Because the image radiance mean $< I >$ may vary over the image it is useful to consider the RMS in small image areas (blocks of the size of the point target filters). The RMS Clutter measure is calculated by averaging the RMS values found in each of these image blocks. Whenever the local radiance average does not depend on position in the image this RMS in principle equals the RMS over the entire image. In this paper we use the RMS Clutter measure based on RMS values calculated by dividing the image into blocks containing 4x4 image pixels.

2. DESCRIPTION OF THE INFRARED DATA

In this paper we present data recorded at two different trials. On 15-2-1990 we obtained data with the UA92 CCIR imager during airborne trials at the North Sea. The UA92 (the latest version of the UA-9090 [1]) records CCIR interlaced frames at 25 Hz in the $8 - 12 \mu m$ band. The Field-Of-View is $5°$ (horizontally) x $3°$ (vertically). These data were recorded on a U-matic videorecorder, and later grabbed into a PC/386 via the DT2851 8 bit frame grabber. The frame resolution results in an IFOV of 0.17 x 0.12 mrad. We have recorded background data at sea states ranging from 0 to 6 at flight levels of $150 - 450$ m. At an altitude of 300 m an elevation angle of $1°$ below the horizon corresponds to a distance of about 11 km and an angle of $2°$ correponds to approximately 7 km. We have selected images from the database recorded between 10^h14^m and 14^h55^m Middle European Time (MET). The calibration of these data are based on the recorded air temperature (of $4°C$) and the RMS radiance variation in clear sky areas compared to the NETD ($0.2°C$) of the thermal imager. The effects of sea state on infrared images will be studied with these data. Together with the infrared recordings data on atmospheric conditions were obtained.

A second set of data was recorded at NATO AC243/Panel4/RSG.5 SIVEX trials in November 1989 in Livorno, Italy. A set of background $8 - 12 \mu m$ sea data was recorded with the same UA92 instrument at an altitude ot 13.4 m above sea level. The data were processed in a similar manner as the data of the airborne trials. Because the camera was fixed accurate time recordings are made and the data and sea clutter can be analyzed in the temporal domain. Besides the temporal behaviour, the relation between sea clutter and elevation is studied. The calibration involves the RMS noise in aereal parts of the images. From the database we selected image sequences recorded on November 3, 1989 at $14^h04^m41^s$ MET (hereafter sequence I) and November 4 at $09^h11^m41^s$ MET (sequence II). Each image sequence contains 2 seconds of data sampled at 12 Hz and 20 seconds of data sampled at 1 Hz. This allows us to study frequencies in the image sequences between 0.1 and 6 Hz.

During the same NATO trials sunglint data were recorded with the six wavelength Multi Path Transmissiometer Radiometer (MPTR-3) of FEL-TNO [2]. At 0.6, 0.8, 1.3, 2.1, 4.0 and $10.0 \mu m$ data were used over a $30°$ area in azimuth and $6.3°$ in elevation. Each azimuth line (originally $60°$) is scanned in 16.67 msec. After scanning upwards the scanner holds the same elevation for about 0.67 sec. for which temporal analysis is possible (similar after scanning downwards). The IFOV of the system is 1.3 mrad. These MPTR data were taken during the SIVEX trials in Livorno at 13.4 m above sea level on November 2, 1989 at $14^h55^m30^s$ MET. These simultaneously measured data were recorded on Bell and Howell 4020A tapes and later grabbed on the PC/386 with the use of the DT2851 frame grabber. Some drift effects needed to be removed with the use of a vertical post on the left side of the images. We have also used MPTR data grabbed directly in the PC/386 between 15^h01^m and 15^h07^m. These MPTR bands were not measured simultaneously and were taken with diaphragms adjusted to the signals at each wavelength independently. The effects of sunglint on sea clutter are described based on these data. Because of the extreme radiances created by reflected solar energy, the calibration of the images is hampered due to a deliberately diminished aperture for which no accurate absolute calibration could be obtained. Therefore these sunglint images are calibrated from 0 to 100 % from the minimum to the peak of the average sunglint pattern. During the SIVEX trials data on the atmospheric conditions were recorded. At at altitude of 13.4 m an elevation of $1°$ below the horizon corresponds to approximately a distance of 770 m and an elevation of $2°$ to a distance of 380 m. For the analysis of all images

described in this section we have defined the elevation of $0°$ to coincide with the horizon.

3. SEA STATE CLUTTER ANALYSIS

Definitions of sea states are based on a set of surface descriptions, such as surface smoothness and wavelength. From the wave slope statistics model of Cox and Munk [3] we derive that higher wind speeds result in higher sea states and a broader distribution of wave slope angles. In this paper we investigate the difference between infrared images at different sea states and the clutter behaviour in these images. From these clutter statistics we derive some potential measures that can be of use for sea state analysis from infrared imagery.

Figure 1 shows the basic data for this analysis. In that figure we display the seven images selected from the database. It is very difficult to select images that are truly representative of a certain sea state. It is also difficult, if not impossible, to select images in which sea state is the only variable. On the other hand we may expect similar atmospheric conditions to be representative of, or connected to a particular sea state. The central parts of the images (produced after averaging) are displayed in gray scales in figure 1. In all sea states below 5 a clear horizon separates the sea from the sky. At sea states 5 and 6 a weak horizon is detected, but the infrared contrast between the sea and the sky is much lower than for the other five sea states. The image of sea state 1 shows bright reflected structures caused by the sun. We would like to point out that the image of sea state 1 has a rather smooth structure compared to 0, 2, 3 and 4, and therefore may be a bad representative of its class. The other five images are more representative examples as will become clear later.

Figure 2 shows elevation profiles of apparent temperatures averaged over $1°$ azimuth intervals over the centre of the infrared images (left scale). Together with the average we present the RMS value in these $1°$ areas (right scale). From figure 2 we derived the following data. The decrease of air temperature with elevation is in the range of -1 to -3 °C/deg, at elevations near zero. This value is very similar in all the images in which it can be determined. At the higher sea states (5 and 6) we find a very flat relation between T_{air} and elevation. This can be the result of the atmospheric conditions (low transmission) during the measurements. The actual visibility during the measurements at these sea states was 12 NM while it was around 30 NM for sea states $0 - 1$, while the relative humidity ranged from $80 - 85$ % for all sea states. In the morning the cloudiness was between 5 and 8 octa, in the afternoon 4 to 5 octa. Below the horizon we find a similar kind of relation as above the horizon. Although sea state 0 has a steep relation (4°C/deg), most sea states (1 to 5) have a moderate relation (1 to 2°C/deg) just below the horizon. Sea state 6 has a completely flat relation with an apparent sea temperature of 0.5°C above the sky temperature.

Concerning the RMS values we find the following characteristics. For each of the sea states 1 and 6 the RMS value is equal at equal elevations. For all sea states except 1 we find a pattern of increasing RMS for lower elevations. We have already noted possible uncertainties that may occur in the image of sea state 1. Just below the horizon the RMS is equal to the RMS in the sky, representing the small amount of structure at these elevations. Because the apparent temperature is nearly constant at equal elevations (ϵ), the RMS as calculated and shown in figure 2 is not very different from the average RMS Clutter measure that is obtained by averaging RMS values in blocks of 4x4 pixels. In figure 3 we show the moving elevation average that is constructed from the latter RMS Clutter measure. The figure is normalized to 10 % of the air RMS. For reasons of clarity we have split the diagram in two. Again sea state 1 is different from the others, that have a slope $-dRMS/d\epsilon$ decreasing with sea state. For the slope we find for sea states 0 through 6 respectively $RMS_{-1°} - RMS_{-0.5°} = 6, 0.2, 2.9, 2.6, 3.7, 0.2$ and -0.7 in units of $RMS_{air}/10$. This shows that there is a trend in the relation between sea state and $dRMS/d\epsilon$.

There are four reasons to explain the noted image differences. Because transmission decreases with distance $(e^{-\sigma d})$ radiance variations in farther areas are diminished. At larger distances pixels will have larger geometrical surfaces and hence will average out wave structure information over a single pixel ($\propto d^2$). At grazing elevations
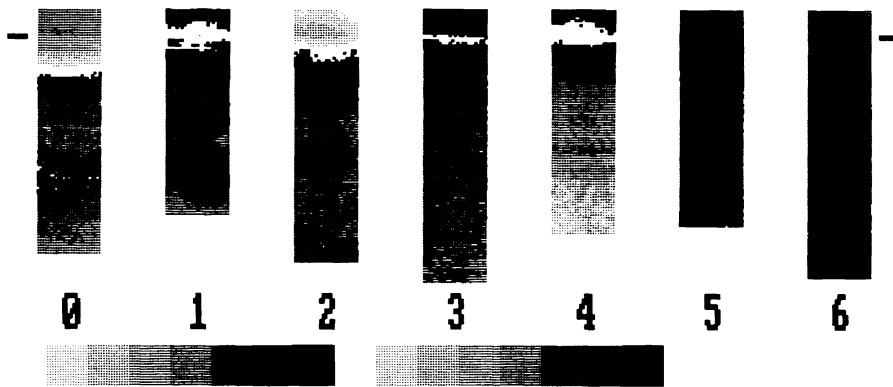
Figure 1: Infrared images (8 – 12 μm) recorded at sea states 0 through 6. Gray scale representations are shown using a double step scale (from white to black) as shown at the lower edge of the image. The image size corresponds to 1° x 3° of the image centre. The labels indicate the sea state number. The horizon is marked by a dash at the sides.
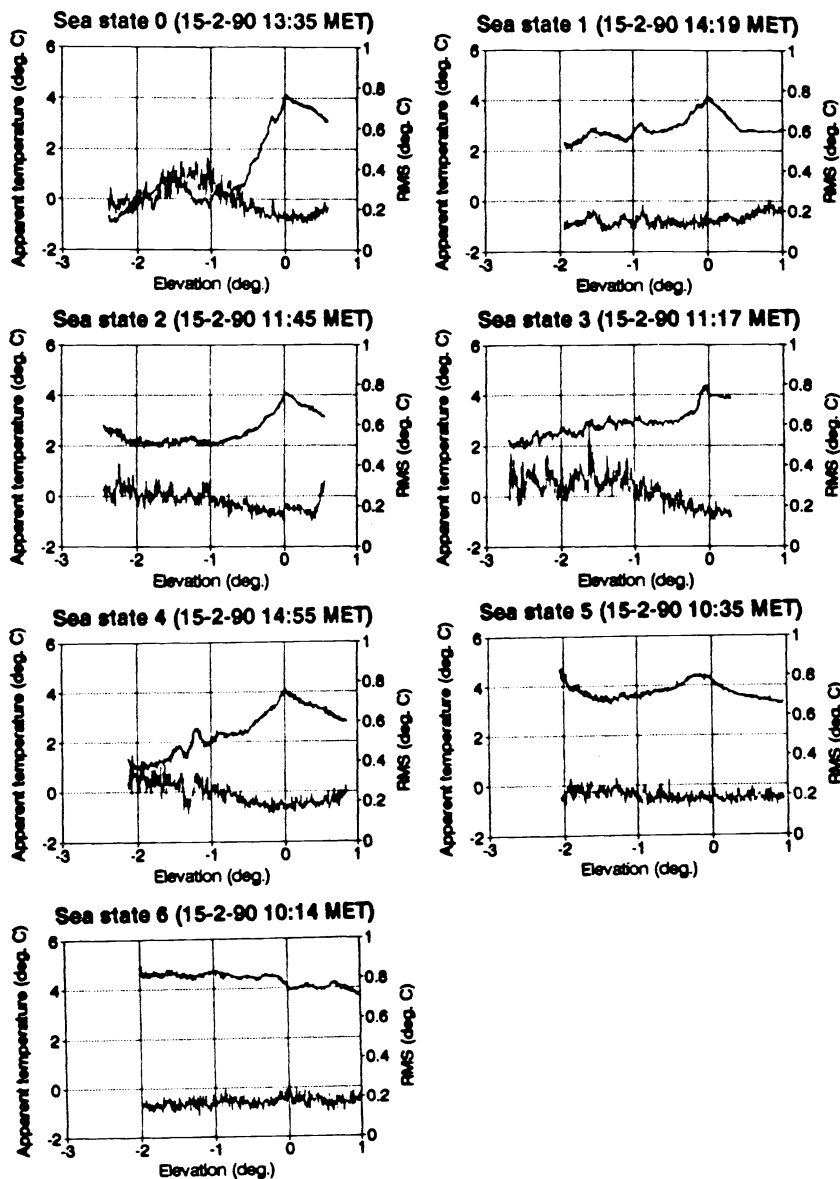

Figure 2: Vertical cross cuts of the images of figure 1. The radiance of the central area was averaged over 1° in azimuth. This average is presented together with the RMS in the radiance.

angles the reflection coefficient increases and there should be a higher contribution of reflected cold sky radiation (note that our vertical FOV $= 3°$). However this does not contribute to a large amount because the temperature of the reflected low elevation sky is relatively high. Hence we do not expect clear differences between different sea state images near the horizon. Areas at the lowest elevations present in the images ($-3°$) are much closer. They reflect colder sky. This is where clear differences in the image radiances and its variations may occur. A change in the reflection coefficients occurs when the top water layer produces more spray. Then the sea will emit more like a true emitter (less reflection) and we observe an apparent temperature which equals the true sea temperature. This effect occurs at higher sea states. This is how we can explain the sea temperatures rising above the air temperature for the higher sea states. The variations in the radiances are reduced due to the lower reflection properties at the higher sea states and hence we expect a lower RMS. To be complete we need to add the effect of a different cloudiness during the measurements that may obscure part of the cold sky. Quantitatively we cannot evaluate the cloudiness effect.

4. TEMPORAL BEHAVIOUR OF CLUTTER

From the UA92 dataset recorded at the SIVEX trials we have selected two image sequences dated November 3, 1989 (Seq. I) and November 4 (seq. II). Figure 4 shows the first image in each sequence, averaged in blocks of 4x4 pixels, together with the local RMS image in those blocks besides it. From the figure we see that the images of seq. I have less clutter than the images in seq. II. In seq. II we see intense variations on intermediate scales. From the images we see that the sky is warmer than the sea in seq. I and colder than the sea in seq. II. During both measurements the recorded wind speeds are similar, however the average of wind speeds during the day of seq. I is 4.5 m/s while for seq. II it is 9.5 m/s. From all appearances the data in seq. II are related to data at higher sea states.

At a set of elevations of $0.2, 0.5, 1.0$ and $2.0°$ below the horizon we averaged local RMS values from blocks of 4x4 pixels in areas of $5° \times 0.2°$. The average time evolution of the RMS is presented in figure 5. We note from figure 5.a that there is a period of $5 - 6$ sec. in the seq. I data at elevation $-2°$. Closer to the horizon we find no clear period. At smaller time scales in figure 5.b we find a period of 0.4 sec. in all elevations presented. Again this period is better visible at the lower elevations. The varying RMS values are related to the wave structure. The peaks in the curves occur at different elevations at different times, with a phase shift approximately linear in elevation angle. The smallest possible phase shifts are resp. 0.22 sec/deg and 1.7 sec/deg (note the ambiguity in phase shifts due to the periodicity). In figure 5.c we do not see a clear period in all four seq. II curves, however there are some peak similarities. In figure 5.d we obtain a period of $0.3 - 0.4$ sec. in all angles, superimposed on a slope in the figure. Phase shifts in seq. II are resp. 0.11 sec/deg and 0 sec/deg. Notice the slope in the first two seconds of sequence II. Because these data are normalized to the RMS in the air there is no calibration effect accounting for the slope. The increase in RMS was not found in the sky RMS, but only in the sea RMS. Because of the presence of phase shifts in the peaks of the RMS Clutter measures, it would be difficult to explain variations by errors or systematic effects in the individual images.

Figure 6 shows two–dimensional histograms of subsequent images in time sequence I. All diagrams have the first image on the horizontal axis and resp. images 2, 5, 23 and 228 on the vertical axes (subsequent images are 1/12 second apart). In each diagram we see two separate areas, at lower radiances (upper left) sea pixels are found and at higher radiance (lower right) sky pixels. When comparing the images the sky area does not seem to change its character. The sea area gets clearly wider with (vertical) image number, and its peak gets less pronounced. This is due to the differences between subsequent images that occur in the progressing sequence. At a difference of 10 or 20 images the histogram shows a broad correlation area. Note the agreement in the size of the correlation area after 23 and 228 images. Two–dimensional histograms of seq. II are not presented but show the same general features, except that in the latter case the sky is colder than the sea and the two ares are more separated.
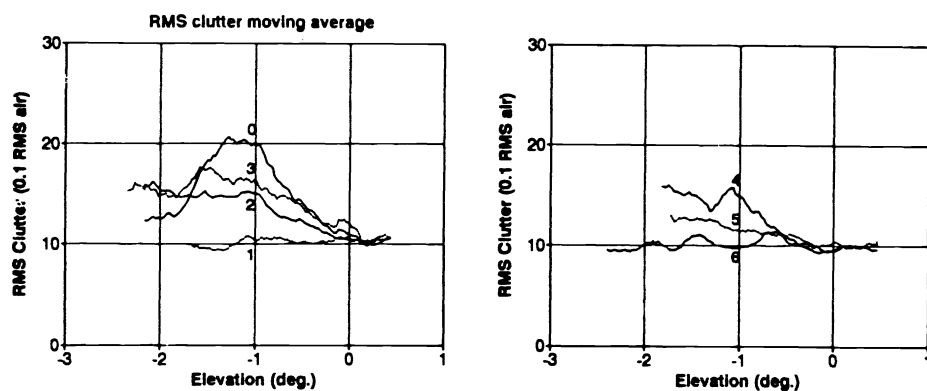
RMS clutter moving average

Figure 3: RMS Clutter moving average pattern for sea states 0 through 6. The labels indicate the sea state number.

03-11-1989   04-11-1989
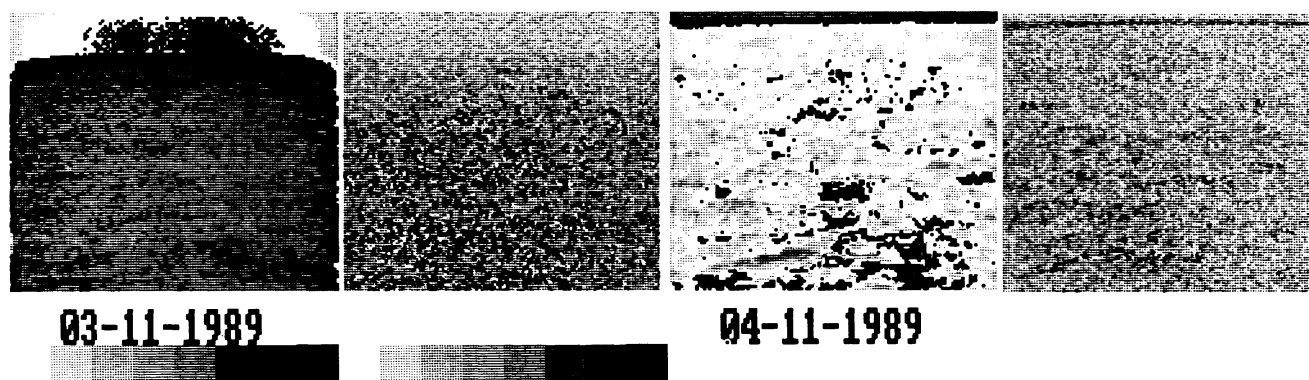
Figure 4: The first images of infrared sequences I and II recorded at the SIVEX trials. At the left we present the average (4x4 pixels) radiance and at the right (10 times) the RMS image (on 4x4 pixels). We have used a double step gray scale function (white to black) presented at the bottom.
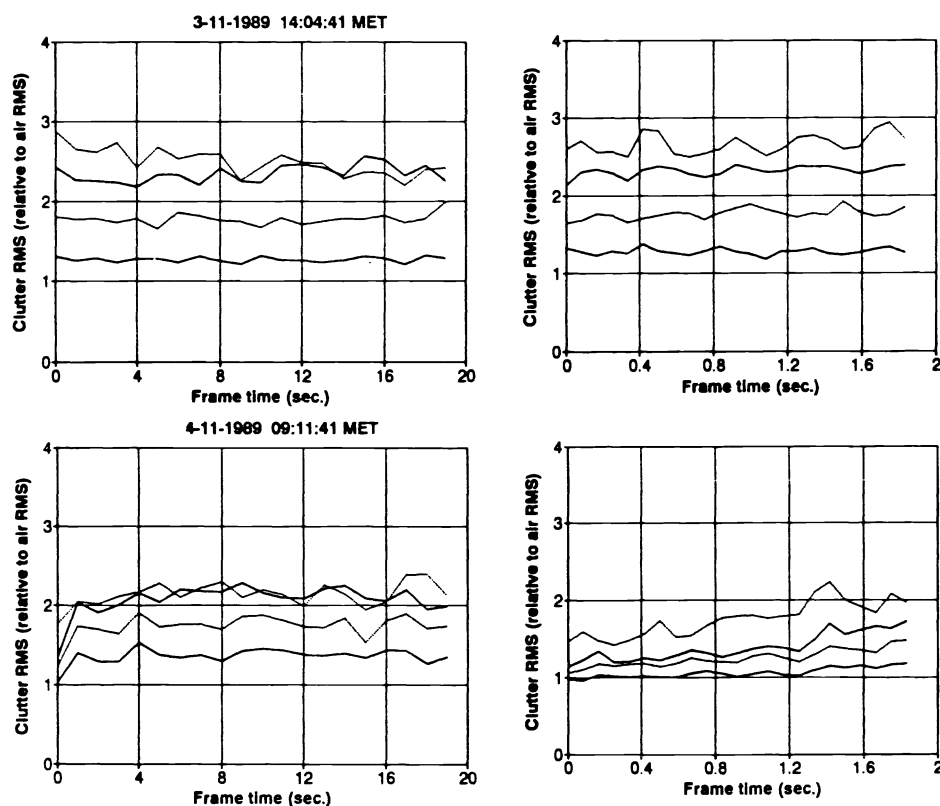

Figure 5: Temporal evolution of RMS Clutter. Sequence I is shown in the upper figures (figure 5.a: for 20 seconds, figure 5.b: for 2 seconds). Sequence II is shown in the lower figures (figure 5.c: for 20 seconds, figure 5.d: for 2 seconds).
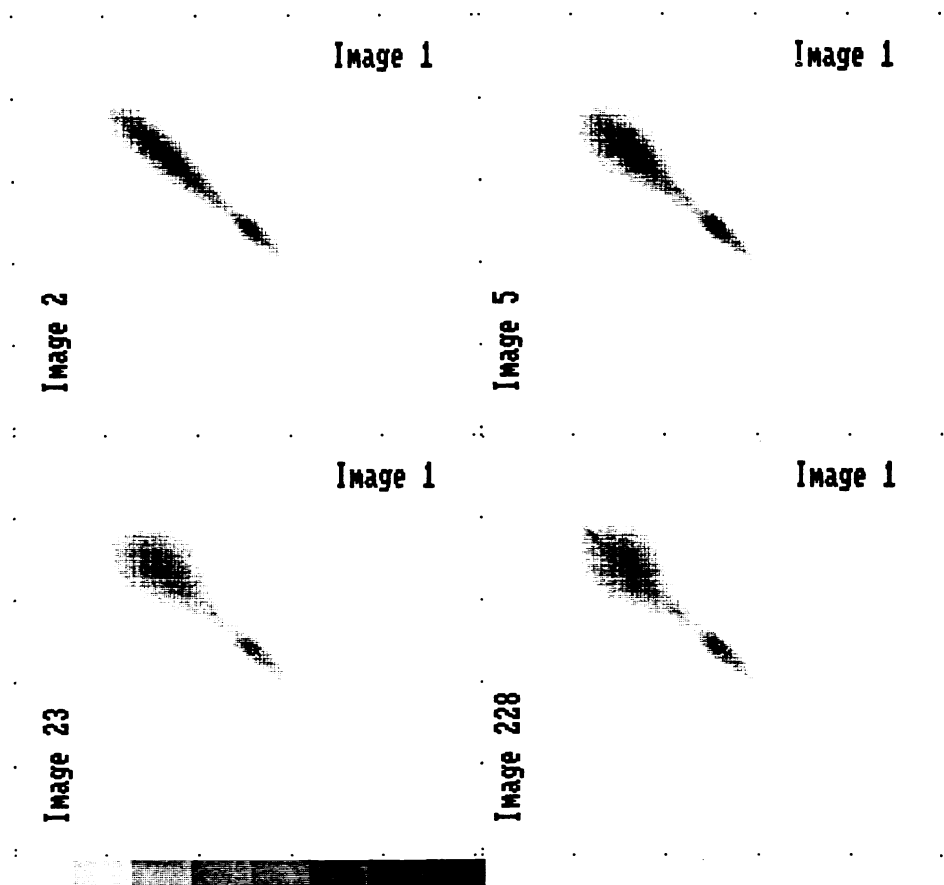
Image 1

Image 1

Image 2

Image 5

Image 1

Image 1

Image 23

Image 228

Figure 6: Two dimensional histograms of image sequence I. The horizontal axis presents the radiance in the first image (number 1) of sequence I increasing rightward from 0 to 255. The vertical axis presents the radiance in images 2, 5, 23 and 228 resp. increasing from 0 to 255 downward. Dots mark each 50 radiance steps. The gray scale bar is presented at the lower edge.
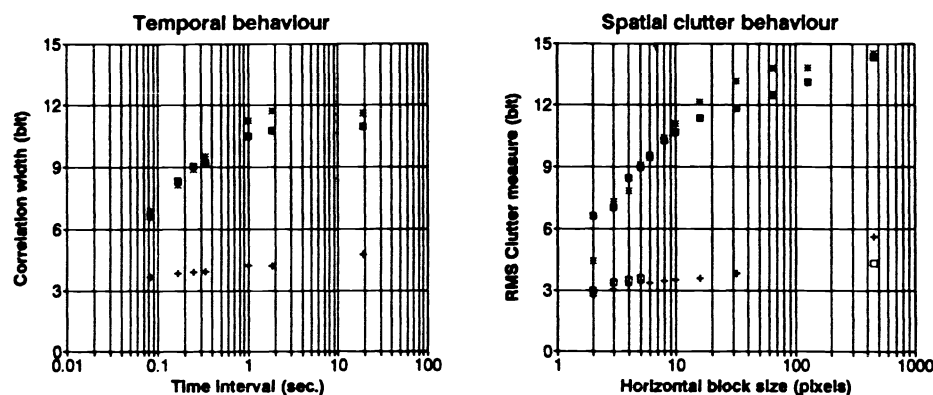

Temporal behaviour

Correlation width (bit)

Time interval (sec.)

Spatial clutter behaviour

RMS Clutter measure (bit)

Horizontal block size (pixels)

Figure 7: Temporal correlation presented by the evolution of the Correlation width at the left (figure 7.a). The right diagram shows the RMS Clutter calculations in square areas of different sizes (figure 7.b). The 1D-size is presented at the horizontal axis. The data at a horizontal block size of 450 pixel show the RMS value of the whole image area. For sequence I ■ represents the sea and + the sky; for sequence II * represents the sea and □ the sky).

From these correlation diagrams we have defined a metric to describe the correlation. We have checked that the average straight line has a slope of 45°. After that we have averaged the 2D–histogram values along the 45° line and used this as a normalized histogram HIS(b) of the distribution of pixels separated by a displacement of b radiance bits from the 45° line. The averages were obtained for the sea and sky areas separately and are approximately Gaussian. We have then calculated the RMS width of the histogram via the expectation value of b^2 via $Eb^2 = \sum_b b^2 \text{ HIS}(b)$, this is equal to the RMS standard deviation σ as the expectation value of b is $Eb = 0$ (on the 45° line). For two perfectly correlated images the 45° line would result in $Eb^2 = 0$; for two normally distributed images $N(\mu, \sigma^2)$, with similar μ and σ, the result will be the value $Eb^2 = \sigma^2$.

The values of the correlation width $CW = \sqrt{Eb^2}$ are given in figure 7. For comparison with CW we show the effect of increasing the number of pixels per block for which we average the RMS. This is shown in figure 7.b. When the blocks are as large as 10x10 pixels the value of CW between $1 < \Delta t < 20$ seconds equals the RMS. This is true for sea and sky data. The increase for larger areas in the RMS is due to the effect of a varying average over the image. From the data obtained we get a quantitative result on temporal correlation. For longer time differences between two images both Eb^2 for the sea and sky areas are increasing by 70 and 25 % resp. The sky value is approximately equal to the RMS in the sky of a single image (figure 7.b). The relatively small increase in RMS of 25 % shows that the image skys are almost entirely unrelated. For the sea the CW values over large time intervals (> 1 sec.) are also close to the average RMS in a single sea image. The RMS in the sea varies from 10 (for average of blocks of 10x10 pixels) to 15 for the entire image. We conclude that the images in each sequence are unrelated when they are more than 1 second apart. An increase in CW of 50 % of the difference $CW_\infty - CW_{0.083sec}$ gives a time constant of 0.3 sec. This value is equal to the short period in the RMS Clutter evolution along a constant elevation in figure 5. We have therefore shown that the metric $1 - CW/RMS$ is a good estimate for the correlation.

Another way to calculate the relation between the images is by making a cross–cut through the sequence datacube along some particular elevation angles. We have chosen 0.5, 1.0, 1.5, 2.0, 2.5° below the horizon. The data of an elevation of 1° below the horizon are shown in figure 8. From the data we see structures extending in time up to 2 seconds (the whole range in figure 8.b). Notice that the upper diagrams show horizontal structures corresponding to the fact that images one second apart are unrelated. From the Fourier transforms that are shown below the images we derive the angle of movements that correspond to the actual observed movement in the sequences. Again the FFT for a 20 seconds sequence shows frequencies in the elevation direction up to the maximum frequency. For a 2 seconds period the FFT pattern is clearly tilted. The slope gets progressively larger for lower elevations coinciding with the fact that the sea wave velocity moves at a constant speed over the surface in the azimuth direction. Note that the slope for sequences I and II is in the opposite direction. For the selected elevations in sequence I the average FFT angles are resp. 2, 2.5, 3.5, 5 and 6.5 degrees, resulting in angular velocities of 1.1, 1.4, 2, 2.9 and 3.7 mrad/sec. For elevations of 1 through 2.5 degrees this corresponds to the distance to the elevation line in the sea for a constant azimuthal velocity of 1 m/s. However for 0.5° elevation we require a velocity of 1.4 m/s. We must contribute this difference to problems in determining the small angle in the FFT at an elevation of 0.5°.

5. SUNGLINT ANALYSIS

Figure 9 shows six simultaneously measured bands of the MPTR scanner during a sunglint experiment. As explained in section 2, the upper half of the image represents an azimuth–elevation image and the lower half represents an azimuth–time image. The spatial half of the image can be distinguished from the temporal part due to the fact that the temporal correlation is larger than the elevation correlation (in the units of figure 9). Sunglint spots occur due to the reflection of solar light by wave facets with the correct slope. The six bands are similar in appearance with the sunglint peak near the right edge and a similar width of the glint pattern. Near the sunglint peak many areas of reflection occur and the temporal image seems to be blurred by a large number of filaments into a few large filaments. Farther from the sunglint peak individual reflections are
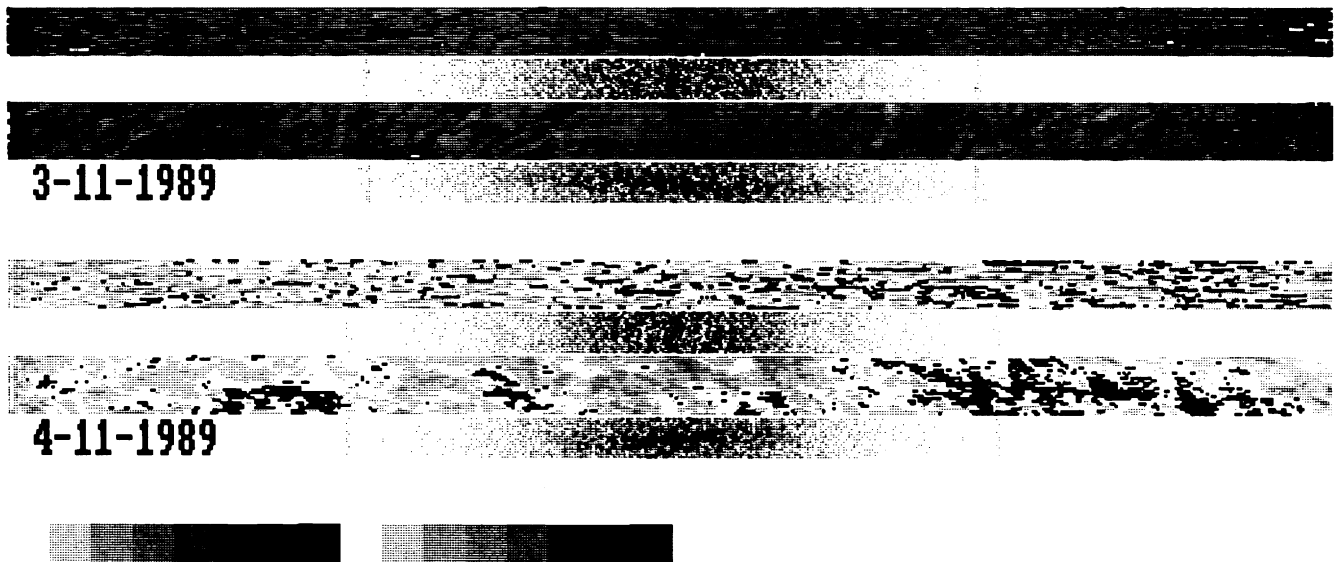
3-11-1989

4-11-1989

Figure 8: Temporal behaviour at elevation $-1°$ in sequences I and II. For both sequences the upper figure is constructed with $\Delta t = 1$ second and the lower with $\Delta t = 0.083$ sec. A single image line is presented for all subsequent images below each other, hence the vertical axis is the time axis. Below each image we present the Fourier Transform of the central image part. The gray scale bar is presented at the lower edge.
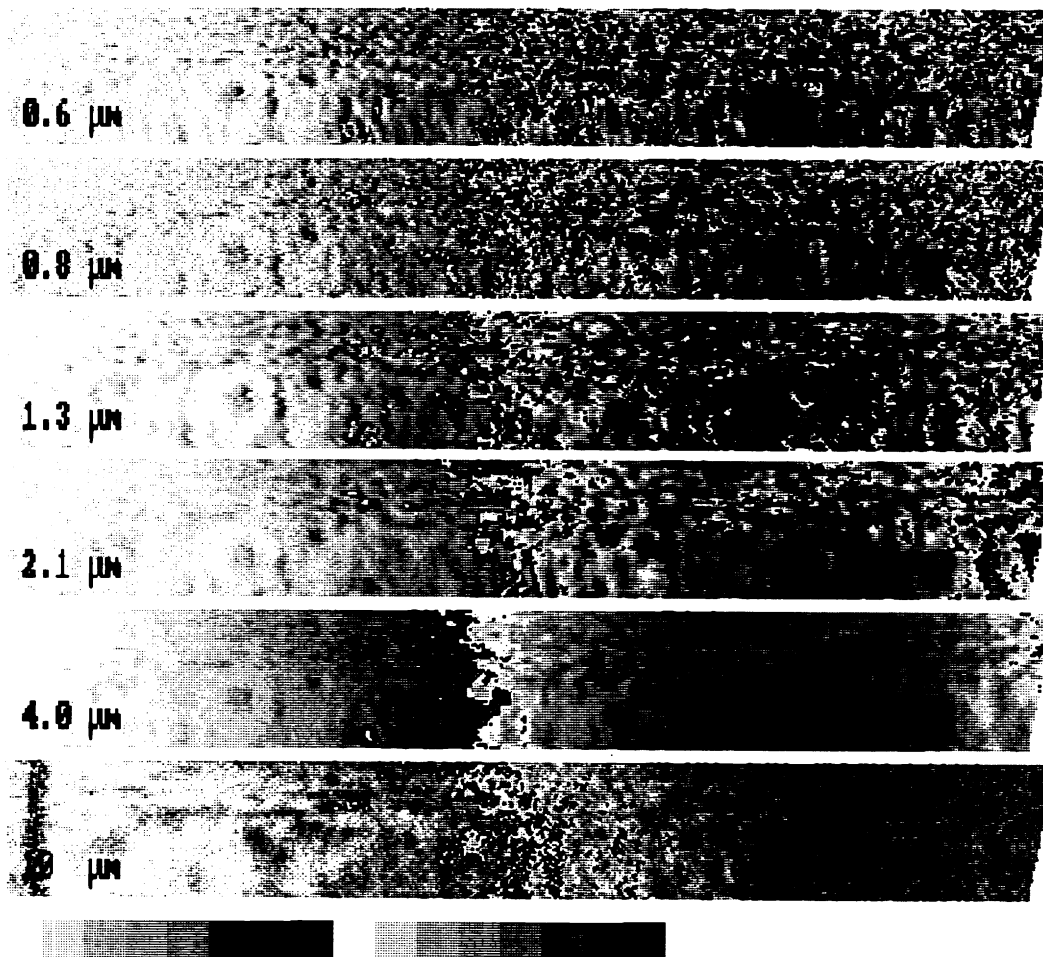

0.6 μm

0.8 μm

1.3 μm

2.1 μm

4.0 μm

μm

Figure 9: Simultaneous MPTR sunglint images at six wavelengths, labeled by their wavelengths. A gray scale bar is presented at the lower edge of the figure. The upper half of each band shows a normal azimuth-elevation image while the lower half shows an azimuth-time image.

identified. Some of these individual features are traced over a number of bands showing spectral correlation between the bands, but this is not always the case. There are resolution differences between the six bands, with the 4 and 10 μm bands having a smoother appearance. This fact hampers a quantitative comparison between the different wavelength bands at full resolution. The 10 μm band seems to show more differences compared to the other five bands, but the sunglint pattern is clearly present.

From a second set of MPTR observations we have determined the average azimuth profile over the elevation area and over the temporal area. The results are shown in figure 10. For each of the six wavelength bands the upper diagram shows the spatial averaging and the lower diagram shows the temporal averaging. In each diagram the upper curves show the azimuth profile averaged over elevation and time resp., while the lower shows the RMS value. With the exception of 10 μm all diagrams show a similar increase in average and RMS near the sunglint peak. The value of the RMS at the sunglint peak equals 0.25 to 0.30 for most bands, but is lower in the 4 and 10 μm bands (resp. 0.13 and 0.20). The elevation averaged profiles have been fitted with Gaussian curves that are represented in all figures. Note that these Gaussian curves fit the average profile well. The time averages clearly show a different pattern from the Gaussian profile and are not smooth at all. Only the 4 and 10 μm time averages do not differ much from the Gausian profiles. In these temporal averages the individual sunglint patterns dominate the profile for a large number of scans and therefore influence the average profile more. The Full Width Half Maximum (FWHM) of the sunglint profile was estimated from the fitted Gaussians and is nearly equal in all bands (8.8 $\pm$ 1.0 °), largest in the 4 μm band.

From the images we have estimated the duration of individual sunglint spikes. In order to do this we have chosen filaments in the temporal domain of the image that are away from the sunglint peak. From the data we derive the same value for the six wavelength bands, ranging from 0.15 to 0.20 sec. This duration time may depend on a number of parameters, as e.g. solar aspect angle. In the sunglint peak small wave slope angles are sufficient to reflect sunlight towards the scanner. Due to their higher probability of occurence we may expect to find a large number of these reflecting wave facets to be present accounting for the temporal blur effect. The mentioned duration time corresponds to about 15 to 20 % of the temporal area in the image, indicating that we may have only five or six independent temporal pixels.

We have estimated clutter values in the different infrared bands at 2.1, 4 and 10 μm for a number of elevations from 0 to 6 ° below the horizon. The data were taken in 1 ° intervals and normalized to the RMS in the area just below the horizon (0 – 1°). For lower elevations we find an increase of RMS values in all three bands. At elevations between 5 and 6 ° we derive values of the RMS of 2.9, 2.4 and 1.4 in the 2.1, 4 and 10 μm bands. At intermediate elevations a similar relation exists. This shows that at fixed elevations the RMS increases more at lower wavelengths. This quantifies the fact that the 4 and 10 μm images are much smoother than the other bands. The solar radiation (5800 K black body) is also relatively less in these two bands.

In order to quantify the relation between the various MPTR wavelength bands we have defined the correlation factor between the bands i and j as $C_{i,j}|-| = \sum | I_i - I_j | / \sum 255$, where we sum over all pixels in a certain image area and I_i and I_j are radiances in images i and j at similar spatial positions. This factor gives the average normalized absolute difference between the two images. Ideally correlated images will result in a correlation factor 0. Figure 11 shows the correlation factor calculated with all possible image combinations. Data correlated with the 10 μm image starts at image displacement –5 (only correlated with images at lower wavelengths), etc. To perform the correlation we used an image area on the slope of the sunglint pattern. We must take care of the average background in the images and the expected value is $C|-| \sim \sqrt{2}\sigma/255$. In general we observe an increasing correlation factor $C|-|$ with increasing image (wavelength) displacements. The variation in the correlation factor is 40% of the maximum value. We have calculated the same ratio for the images that were recorded non–simultaneously and we get a variation of only 13% of the maximum value. These maximum values cannot be compared directly. The fact that this ratio is 3 times higher in the first case reflects the better correlation between the images in that case, compared to the second case. However this
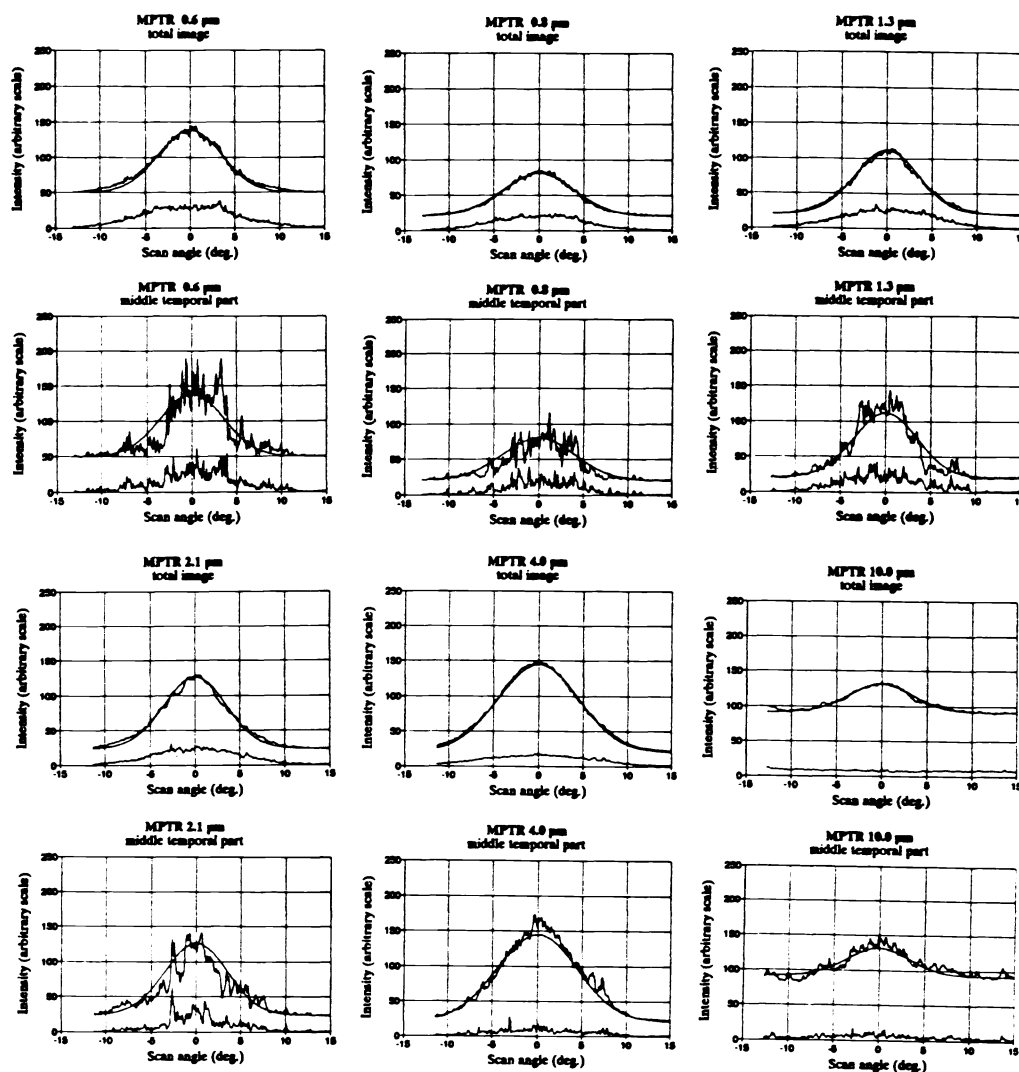
Figure 10: Average sunglint pattern at six MPTR wavelengths (non–simultaneous). The profile averaged over elevation is given in the upper diagrams; the profile averaged over time is given in the lower diagrams. Together with the average (upper curve) we present the RMS (lower curve) and fits Gaussian through the elevation–average profile.
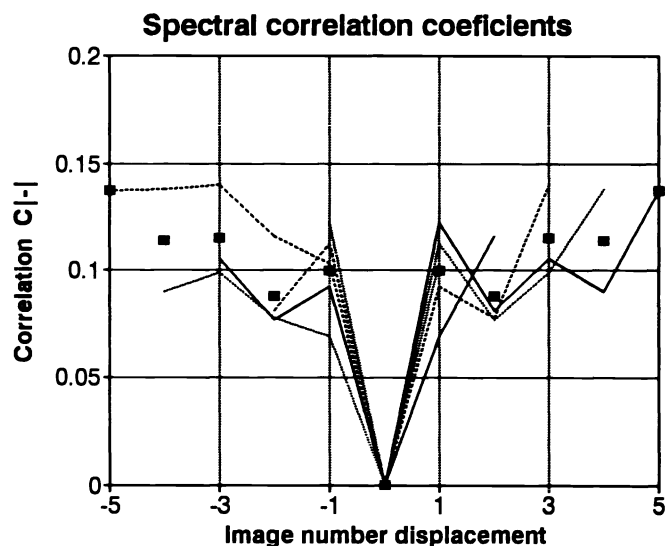

Figure 11: Spectral correlation coefficients $C|-|$ of the MPTR sunglint data. Data of all bands are used. Images that are correlated with the first band at 0.6 μm (solid line) range from 0 to 5 image number displacements (there exist only higher wavelengths), while images correlated with the 10 μm band (dashed) range from –5 to 0 image displacement numbers. The symmetric ■ present the averages of all data for a single image (wavelength) displacement value.

behaviour does not hold for all values of the correlation factor but it is only a general trend. Figure 11 shows that data related to the $10\,\mu m$ band shows higher values than for the other five bands. This may be related to the fact that this $10\,\mu m$ band shows more differences with respect to the other five bands.

6. CONCLUSIONS

The data presented in this paper show quantitative results on the analysis of infrared marine backgrounds. We will continue to investigate sea background data in a similar way as described here.

We have presented infrared $10\,\mu m$ images recorded at sea states 0 through 6. Elevation profiles were constructed of the average radiance and the RMS values. The data show that the RMS slope $-dRMS/d\epsilon$ between elevations of 0.5 and 1 degree decreases for increasing sea state. Hence elevation RMS profiles of infrared images can give valuable information on sea states. In order to quantify the relations between infrared imagery and sea states more work is needed to select a completer set of characteristic images for certain sea states and to diminish other atmospheric effects.

On the basis of two time sequences we have calculated the temporal and spatial behaviour of the clutter RMS. We have determined certain short periods in the RMS of 0.3 – 0.4 sec. We have interpreted the width of the 2D–histograms of radiance as correlation widths that represent a metric for the temporal correlation in image sequences. After 1 second in time both image sequences are uncorrelated. From FFT data of the evolution of a single line, azimuthal angular wave velocities have been calculated from data and agree with a single linear velocity.

Sunglint patterns are presented in six wavelength bands. Images of simultaneously measured patterns are very similar. Profiles averaged over elevation show a Gaussian distribution of radiance with a similar pattern width ($8.8\,°$). Typical correlation times are estimated to be of order 0.20 sec. Spectral analysis shows some degree of correlation between the images but does not give a clear quantitative relation.

7. ACKNOWLEDGMENTS

8. REFERENCES

1. USFA BV: 1981, Thermal Aiming and Observation System UA9090, Product information doc. 10.0010–E–0282, Eindhoven, The Netherlands

2. A.N. de Jong, M.J.J. Roos: 1987, Description of the MPTR system; Multi Path Transmissiometer Radiometer (Final Report on Project DAJA 45–85–C–0040), FEL 1987–14, The Hague, The Netherlands

3. C. Cox, W. Munk: 1954, "Measurement of Roughness of the Sea Surface from Photographs of the Sun's Glitter", Journal of the Optical Society of America 44, pp 838–850